

IAC-24-B4,7,14

TOM - Advances in Formation Flight and Data Processing

Johannes Dauner^{a*}, Lisa Elsner^a, Tom Geiger^a, Peter Janotta^a, Joshua Redelbach^{a,b}, Klaus Schilling^a

^a Zentrum für Telematik e.V., Würzburg, Germany

^b University of Würzburg, Germany

* Corresponding Author, johannes.dauner@telematik-zentrum.de

Abstract

Formations of small satellites enable remote observation of Earth's atmosphere and surface from multiple directions simultaneously. This approach provides unprecedented perspectives on processes such as volcanic eruptions and resulting ash clouds. The Telematics Earth Observation Mission (TOM), conducted by the Center for Telematics (ZfT), aims to demonstrate photogrammetric observation of these phenomena using a formation of 3U+ CubeSats.

The photogrammetric evaluation of recorded image data heavily relies on precise temporal synchronization across all three satellites. To ensure suitability for subsequent scientific processing, the time difference between photos taken by different satellites must be minimized, ideally within a few milliseconds. Given that the camera data also serves image-based attitude control, meticulous timing of image capture becomes paramount to enable concurrent data usage. Multiple tests with an external time reference show that time synchronization and accuracy requirements are met by TOM's camera and payload computer.

In pursuit of precise and coordinated target pointing, a distributed image-based attitude control approach for relative pointing control was developed, as previously introduced. Additionally, a novel image-based navigation method is planned to be tested during the TOM mission. This method enables precise determination of the satellite's position and attitude in the inertial frame by matching known ground control points (GCPs) stored in an onboard database with corresponding points identified in the satellite's camera images.

To evaluate the different modes of TOM's attitude and orbit control system (AOCS), as well as the control and navigation capabilities across all satellites in the formation, a multi-satellite test environment was designed, comprising configurable elements tailored for various scenarios. The performed simulations and tests show promising results. Further extensions are currently being implemented to include additional aspects in upcoming tests.

Furthermore, the pipeline for photogrammetric processing of the image data obtained by the TOM satellites is presented. This photogrammetry pipeline enables the creation of 3D captures from only a single combined image acquisition of all three satellites as a snapshot in time.

Keywords: CubeSat, Formation Flying, Attitude and Orbit Control System (AOCS), Visual Servoing, Earth Observation, Photogrammetry

1. Introduction

The ongoing miniaturization of electronics enables the design of cost-efficient nanosatellites, revolutionizing their capabilities to perform demanding tasks. Complex missions, e.g. for telecommunications or Earth observation, can now be realized by constellations of formations of small satellites, significantly lowering costs and risks in comparison to single-satellite realizations.

Especially Earth observation missions benefit from the improved spatial and temporal resolution provided by a formation of multiple satellites which coordinate their camera captures [1–5].

A mission utilizing these new possibilities is the Telematics Earth Observation Mission (TOM), aiming to use photogrammetric methods to create 3D Earth surface images. This mission is carried out by the German research institute Center for Telematics

(ZfT). The three TOM CubeSats will establish a formation and synchronously monitor target areas on the Earth's surface from different viewing angles [6–8].

The present work is structured as follows. First, an overview of TOM is given in chapter 2. Next, the satellite bus (chapter 3) and the payload (chapter 4) are described. Chapter 5 explains TOM's Attitude and Orbit Control System (AOCS) modes. Afterwards, a novel image-based method for cooperative tracking of Earth targets which utilizes the images captured by the payload camera is introduced (chapter 6). In chapter 7, the test environment used for the overpass tests and the test results are discussed. Chapter 8 introduces the photogrammetric processing pipeline for the image data provided by the TOM satellites. A variation of the image-based cooperative tracking approach which enables the image-based determination of a satellite's attitude and position is described in chapter 9. Conclusion and outlook (chapter 10) finalize the present work.

2. Mission Overview

The main scientific mission objective of TOM is the monitoring of volcanic ash clouds to capture image data with high spatial and temporal resolution for the photogrammetric reconstruction of 3D models of these ash clouds. This will provide valuable information to improve ash cloud dispersion models, allowing to mitigate the hazard of ash clouds especially for aviation [9]. To fulfill this mission objective, different challenges have to be addressed:

The first challenge is the positioning of the three satellites in a fitting formation to monitor the observation target from different viewing directions at the same point in time. Solutions to this formation flying task are described in detail in [8].

To ensure sufficient image overlap for the application of photogrammetric reconstruction methods, very precise and coordinated pointing by all three satellites in the formation towards the observation target is required. To achieve such a precise attitude control accuracy, TOM aims at demonstrating a novel image-based control approach for cooperative tracking of Earth targets, utilizing the satellites' cameras and their inter-satellite link (ISL) capabilities to minimize the relative pointing error between the satellites in the formation. This cooperative tracking approach, also referred to as *relative visual servoing* is explained in chapter 6.

Another challenge is the exact timing of the image captures across all three satellites since volcanic ash clouds often exhibit very rapid dynamics. Therefore, timing differences in the range of only some milliseconds are desired, which poses a challenging requirement for the synchronization of image capturing, especially since the cameras are also used for attitude control in parallel. The scheduling and synchronization strategies for camera captures are presented in chapter 4.

TOM is the Bavarian contribution to the Regional Leaders Summit (RLS) funded Telematics International Mission (TIM) project, where several international space research institutes work together to create a joint cooperation. The TIM Ground Station Network (GSNW) will span five continents and enable frequent contacts to support the missions of the partners involved. The three TOM CubeSats are currently planned to be launched in 2025.

3. Satellite Bus

The TOM satellites are based on a 3U+ CubeSat platform which adheres to the UNISEC Europe standard for electrical interfaces* (see [10]). This CubeSat platform has been developed by ZfT and provides modular subsystems, redundancy, and a distributed Electrical Power System (EPS) architecture. The CAD model of the TOM satellites is depicted in Figure 1.

TOM's flight-proven onboard computer (OBC) is the central brain of the satellite, utilizing two microcontrollers to provide hot redundancy, additionally monitored by an external watchdog. For communication between the ground station and the satellites, two communication channels are used: UHF for Telemetry and Telecommand (TM-TC), and S-band for payload data downlink (e.g. image data). The three TOM satellites will also communicate directly with each other via a UHF-based inter-satellite link (ISL), which has already been demonstrated during ZfT's NetSat mission [11]. This direct link between the satellites in the formation allows for autonomous formation flying as well as cooperative pointing towards Earth targets.

ZfT's AOCS builds on a distributed integrated modular architecture to ensure fast, accurate and reliable performance of the subsystem. The central processing unit of the AOCS is a redundant single-core ARM microcontroller unit (MCU), which uses a real-time operating system (RTOS) for guaranteed timing performance of the different processing tasks.

*<http://unisec-europe.eu/standards/bus/>

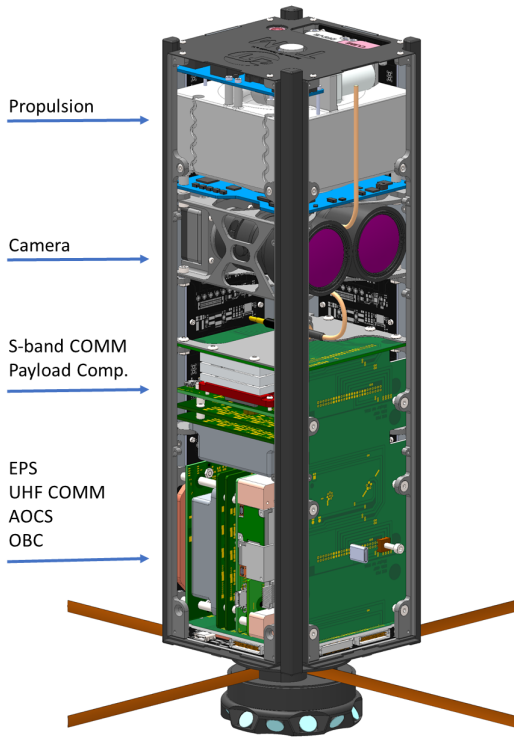


Fig. 1: CAD model of the TOM satellites.

The satellite's five panels each accommodate their own MCU for pre-processing and component control tasks. The central MCU and the five panel MCUs are connected via the UNISEC bus for fast communication between the different AOCS components. The modular approach enables to accommodate a mission-specific set of sensors and actuators, enabling attitude control as well as orbit maintenance and formation flying capabilities in the case of TOM. The following components are directly connected to the central MCU:

- Inertial Measurement Unit (IMU) with a three-axis gyroscope and a three-axis magnetometer
- Six miniature reaction wheels, placed as redundant pairs for each of the three body axes
- Propulsion unit with a bi-propellant thruster and tanks for propylene/propene (C_3H_6) as fuel and nitrous oxide (N_2O) as oxidizer, providing a total impulse of 405 Ns

The five panels each house the following sensors and actuators:

- IMU with a three-axis gyroscope and a three-axis magnetometer
- Magnetorquer
- Global Navigation Satellite System (GNSS) module (only on the four big panels)
- Miniaturized CMOS camera-based Sun sensor (only on the four big panels)

In addition, the AOCS incorporates a Linux-based computing board used to perform mission-specific processing tasks which are computational demanding, like trajectory planning and formation control calculations.

4. Payload

The payload, developed inhouse by ZfT, handles precise and synchronous image capture on all satellites, as well as image data handling, image processing and camera control from ground. In addition, the image-based algorithms described in chapters 6 and 9 are also performed on the payload computer. In case of the cooperative tracking, the resulting angle errors are fed to the AOCS subsystem for attitude control.

4.1 Hardware Overview

The satellite's payload consists of a camera module and a Linux-based payload computer in a redundant configuration (see Figure 2).

The camera module itself consists of a Sony IMX 250C global shutter CMOS sensor and a 100 mm focal length lens. This configuration provides the in-orbit specifications depicted in Table 1.



Fig. 2: Redundant payload camera setup.

Resolution (H×V)	2432×2048
Ground sampling distance (GSD)	18.1 m
Field of view (FoV)	4.8°

Table 1: Payload camera specifications at 525km altitude.

The payload computer is powered by a Broadcom BCM2711 quad-core Cortex-A72 64-bit processing unit, with a frequency of 1.5 GHz, which offers a powerful base for fast image processing.

Both hardware components were tested for radiation hardness and survived a Total Ionizing Dose (TID) of 33 kRad [7].

4.2 Timing and Multi-threaded Processing

In order to fulfill the precise timing requirements of TOM, the payload subsystem has to efficiently manage the commanded image capture times as well as the available resources of the payload computer to process the image data. The camera driver software (further details are provided in [12]) uses the internal UTC time of the payload computer, which is set by the underlying Operating System (OS), as a reference for all captures. The synchronization of multiple payload systems is managed by this OS and secures the requirements on synchronicity by matching their internal system time.

Due to the multiple cores available on the payload's CPU, true multi-threading can be used to improve the performance of the image capture process. In specific that refers to the rate at which images can be taken, as well as the absolute accuracy of the timestamps and their consistency.

The payload's subsystem driver utilizes four different threads to perform its tasks. One thread handles the actual image capture, one performs all image processing and file management, another thread handles the visual servoing process and the fourth thread runs the main housekeeping functionalities of the OS. The thread schedule for a typical operation of the payload is depicted in Figure 3. It can be clearly seen how the division of task execution in multiple parallel threads can increase the maximum rate at which images can be taken.

Another important advantage of the multi-threading approach is the possibility to precisely time desired task execution by resuming the respective thread at a commanded time or after another task is completed, e.g. after image data is available. To avoid data corruption, the relevant image data is protected from multiple accesses at once by a mutual

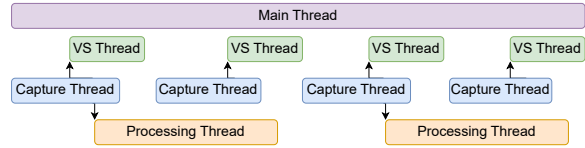


Fig. 3: Typical thread schedule of payload camera operation.

exclusion lock.

4.3 Test Setup and Results

To evaluate the performance of the payload's camera driver, three criteria are considered: absolute performance (specifically capture rate limits), absolute timing accuracy of one image's timestamp compared to commanded UTC time and relative time synchronicity between multiple subsystems in formation [12].

For the performance test, the camera is pointed at a target at a reasonable distance (~ 3 km) and run at conditions similar to a real-world scenario. The image capture rate is increased until a stable limit is found at 10 Hz for visual servoing captures and 5 Hz for normal captures including on-board image processing.

The absolute timing accuracy test utilizes an external UTC reference clock displayed on a high refresh rate screen captured by the camera. The commanded capture times are compared with the external reference time on the respective image with a resulting average difference of (7.0 ± 5.9) ms.

For evaluation of the relative time synchronicity between multiple payload systems, the previous test is conducted for two identical systems in parallel. The expected synchronicity error between the two root from two possible causes: Either it is caused by different image capture execution times on each individual payload system, or it is caused by an offset between both systems' internal UTC times, caused by the time synchronization of the underlying OS. To find out which error source is the most relevant, two test sequences are performed for both payload systems in parallel. To also evaluate the consistency of the results over time, the same test is repeated, separated by 30 min. After the first sequence, both internal clocks are synchronized again with the underlying OS and the test sequence is repeated. Analyzing all four tests on the time difference between the two system's images, both camera subsystems capture images highly synchronously compared to the external UTC reference clock with

only a constant offset apparent in a low double digit millisecond range. Both offsets are also consistent and stable after the time separation of 30 min. This leads to the conclusion that the limiting factor of both system's synchronicity is the internal UTC time synchronization and not the payload's subsystem driver, as this would lead to a more unstable time difference, which could not be observed.

5. AOCS Modes

The design of the TOM's Attitude and Orbit Control System (AOCS) is based on QUBE's Attitude Determination and Control System (ADCS) [13]. The AOCS is extended to allow coordinated position and attitude control in a formation. In addition to the ADCS mode manager, an Orbit Determination and Control System (ODCS) mode manager is added to separate attitude and position control tasks. On top of that a new hierarchy level is introduced, the AOCS mode manager, which handles the interaction between the different ADCS and ODCS modes and defines the allowed transitions. The AOCS modes are shown in Figure 4.

The command mode is a manual mode, where all components and autonomy are deactivated, and allows the operator to turn on e.g. sensors, actuators or filters manually.

The safety mode serves as a fall-back mode in case errors could not be recovered in the nominal mode. Similar as in the command mode, all components are deactivated. Leaving this mode is only possible via the operator.

In the nominal mode the ADCS switches between detumbling and Sun pointing to either reduce the satellite's rotation rate or to orient the solar panels toward the Sun to charge the batteries. The ODCS is transitioning between localization mode and planning mode. In the former, position data of the satellite is calculated using orbit propagators (Simplified

General Perturbations 4 (SGP4) [14], Deprit's Radial Intermediary (DRI) [15] [16]) or GNSS data. In the planning mode the ODCS is preparing the upcoming orbit maneuver, e.g. calculating the required attitude for the point in time where the thrust commands need to be executed.

In the orbit maintenance mode the ADCS is in local Radial, Transverse, Normal (RTN) pointing mode, where the attitude is controlled in a way to orient the thruster in the required direction. The ODCS is switching between planning and control mode. In the control mode, the thrust commands are executed to adjust the positions of the satellites within the formation.

In the image downlink mode, the AOCS coarsely orients the antennas towards the ground station in Würzburg to enable downlink of the payload data via an S-band communication unit. The ADCS is in Latitude, Longitude, Altitude (LLA) pointing mode and the ODCS stays in localization mode, ensuring continuous tracking of the ground station.

The joint observation mode makes sure that all three satellites are observing the same target area on ground, fulfilling the mission's objective. The ADCS switches into the pointing mode to track the target area on ground and the ODCS stays in the localization mode to provide accurate position data. The ADCS's pointing mode starts with absolute tracking and then switches to relative tracking to further refine the image overlap. The control loop is shown in Figure 5.

In the absolute tracking the satellites will track the observation target independent of each other in LLA pointing mode. Sun sensor, magnetometer and gyroscope are used to determine the actual orientation of the satellite. The tracking guidance calculates the desired orientation based on the current position of the satellite. This information is fed into the tracking controller [17] to calculate a torque in all three axes. This torque is forwarded to the reaction wheels, which adjust their speed accordingly to compensate for the control error.

The relative tracking mode is implemented by using an image-based attitude control approach, called relative visual servoing. Image features are extracted, exchanged between the satellites and continuously tracked to calculate the control error. This technique still requires an initial independent coarse alignment towards the target and it also necessitates a role assignment of the satellites. The leader satellite determines the features to be observed and distributes the data to the two follower satellites,

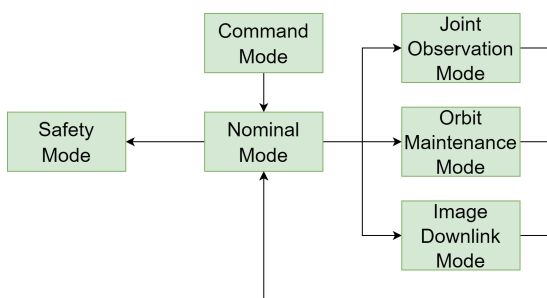


Fig. 4: AOCS Modes of the TOM formation.

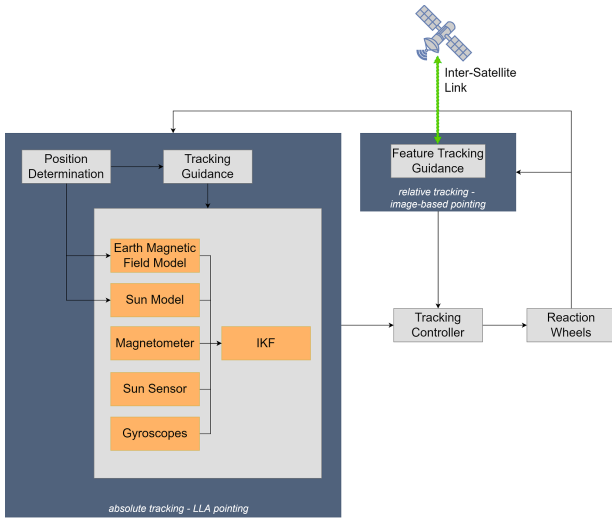


Fig. 5: Control loop of the joint observation AOCS mode.

which then need to match their features with the features of the leader to track the same target area. The features are directly obtained from the images of the payload camera, avoiding the need to integrate an additional sensor. More details about the relative visual servoing can be read in the following chapter 6.

6. Image-based Cooperative Tracking

To achieve the required overlap of the images, the fine pointing of the TOM satellites towards the observation target is coordinated based on the image data itself. Image-based control methods originate from the field of robotics and are often referred to as *visual servoing* [18–20]. In the presented method, the pointing of the satellites is controlled relative to each other, therefore this method is referred to as *relative visual servoing*. A deeper insight into the relative visual servoing approach is provided in the work of Dauner and Elsner [21].

6.1 Visual Servoing Fundamentals

The base principles of visual servoing in the scope of the presented work rely on the detection and matching of features in satellite imagery. Features are highly distinctive points which can be detected repeatedly and reliably in different images showing the same scenery, e.g. from varying directions or distances, and even when parameters like brightness or exposure change [22].

To detect and locate features in an image, detection algorithms search for areas with unique

structural information and specific shapes, like edges or corners. This is achieved by defining a certain salience measure, like pixel intensity gradient, and identifying local extrema across the image pixels.

To enable the comparison of features found in different images, a unique signature for each feature must be created. Feature description algorithms encode interesting information of the considered pixel's neighborhood into a descriptor vector which acts as a numerical fingerprint. These fingerprints also have to be robust to noise and to changes in viewpoint and in photometric imaging conditions [23].

To identify corresponding features in two images, the associated sets of descriptor vectors are compared. After this feature matching, only features present in both sets should remain. The matching is achieved by calculating the Euclidean or Hamming distance between all feature descriptors of both sets. For each vector in the first set, its nearest neighbor in the second set regarding descriptor distance is searched [23]. Since not every feature from the first set is guaranteed to appear in the second set, mismatches with similar features located elsewhere in the image scenery are unavoidable.

To eliminate these false matches and ensure more reliable feature matching, additional checks must be performed during feature validation. The plausibility of all matches is evaluated based on various properties, such as by applying outlier removal algorithms like the RANSAC algorithm [24].

For detecting and describing features, several algorithms already exist, such as SURF [25], ORB [26], BRISK [27] and FREAK [28]. For image processing, Open Source Computer Vision Library (OpenCV) is used which offers implementations for all algorithms mentioned above [29].

6.2 Algorithm Description

The relative visual servoing approach builds on a leader-follower principle, as exemplified in Figure 6. Before the overpass over the ground target starts, one of the three TOM satellites is chosen as leader, which specifies the target area that should be observed by all satellites in the formation. The remaining two satellites are assigned the role of the followers – their task is to point to the target area defined by the leader.

At the start of the overpass over the observation target, the conventional attitude sensors are used to perform a coarse pointing. As soon as the coarse pointing to the target is established, the relative

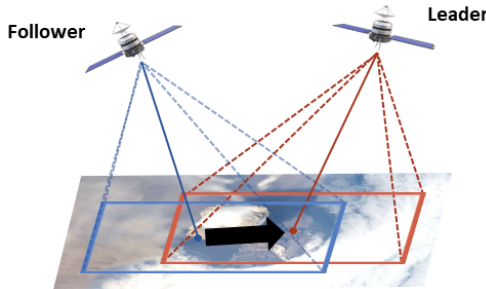


Fig. 6: Leader-follower principle of relative visual servoing.

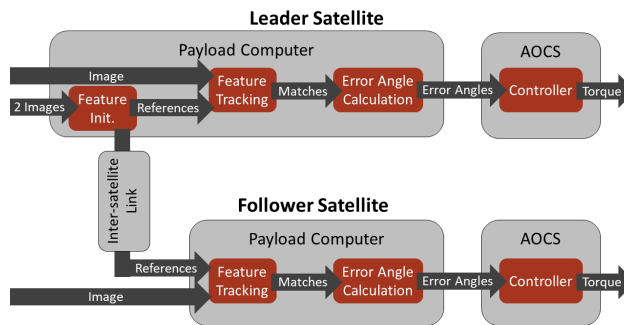


Fig. 7: Main processing steps of relative visual servoing.

visual servoing procedure is started.

The main processing steps of relative visual servoing for TOM are depicted in Figure 7. In the feature initialization step, the leader identifies features in the first two camera images. Those features are used as reference features for the following steps, which are performed onboard all three satellites. Therefore, they are sent via the ISL to the follower satellites. The image positions of the reference features are tracked in newly captured pictures to compare them with their initial image positions. The resulting pixel shifts enable the calculation of the error angles around roll, pitch, and yaw. While these image processing steps are conducted on the payload computer, the calculation of the torque to be applied by the reaction wheels is done by the AOCS, e.g. by a quaternion-based linear-quadratic regulator (LQR).

7. Overpass Tests

7.1 Existing Test Environment

The architecture of the distributed testbed is illustrated in Figure 8. It consists of a

Hardware-in-the-Loop (HiL) simulation framework, the turntable, a 3D-visualization and an Earth Observation Simulator (EOS). Mode details about the distributed testbed can be found in [30].

The simulation framework is written in Java and builds up on Orekit [31]. Orekit provides the orbital state including position and velocity, as well as environmental parameters such as the local magnetic field and atmospheric density or the direction towards celestial objects like the Sun. These states serve as inputs for a user-defined model of the flight attitude dynamics and the associated ADCS sensor and actuator models. The Java library Hipparchus is used for the mathematical and statistical components [32]. The simulation framework loads a scenario configuration and provides it to the simulation core. The core propagates the satellite's orbit and attitude state. Based on this, it can virtualize different components, such as sensors or actuators, making it adaptable for various testbeds where certain components may be absent. It therefore also offers the possibility to perform pure Processor-in-the-Loop (PiL) tests, which is very helpful to keep the complexity low in the first test phases and then gradually increasing it to integrate more and more real sensors and actuators.

Figure 9 shows an exemplary test setup, where mock-up satellites are mounted on both turntables, which orient the satellites according to the simulation framework's propagation. The 3D-visualization is updated with the satellites attitude \vec{q}_s , position \vec{p}_s and corresponding time t to visualize the satellites in orbit.

An exemplary screenshot of the tracking of a target with the TOM formation is shown in Figure 10a. In addition to this, an EOS [33] was integrated for the AOCS test campaign for the TOM mission. The EOS receives the same data as the 3D-visualization to show the camera perspective of the satellites.

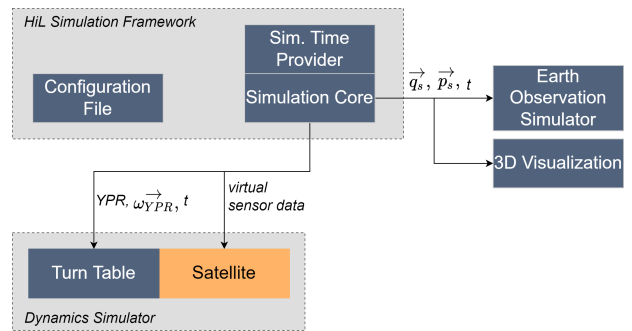


Fig. 8: Architecture of the distributed testbed.



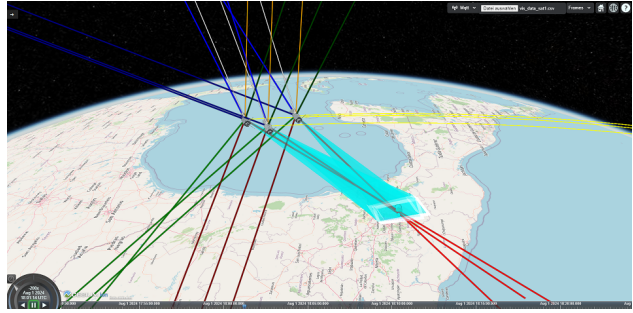
Fig. 9: Turntables with mounted mock-up satellites during relative visual servoing test.

The camera settings can be adjusted in the EOS to display images with the same resolution and FoV as expected from the real cameras in orbit. In Figure 10b, a screenshot of the EOS is shown, displaying the camera perspective of one of the TOM satellites during an overpass.

7.2 Joint Observation Mode Tests

The absolute pointing accuracy of the AOCS's joint observation mode for the TOM mission was evaluated with the distributed testbed described in section 7.1. We began by evaluating the LLA pointing mode of the ADCS to verify that the pointing of the satellites provide enough image overlap to perform the relative image-based attitude control approach described in chapter 6. In this test, the testbed was used in a pure PiL setup where the AOCS subsystem was plugged into the DevBoard and connected to the simulation framework. The flow chart of this test is shown in Figure 11 where all simulated components are marked blue and all real components that were running on-board the AOCS subsystem are marked green. The sensor inputs as well as the reaction wheels are simulated in this test, where its models are configured with the expected and measured inaccuracies.

The volcano Popocatépetl served as observation target (geocentric coordinates: longitude = -98.62° , latitude = 19.02° and altitude = 2725.0m). The reference orbit was chosen as Sun-synchronous orbit (SSO) with Longitude of the ascending node (LTAN) 11:30, an inclination of 97.4975° and an altitude of 525 km, to be similar as expected in the TOM mission. The satellite formation was generated around the given reference orbit, defined as relative orbit elements (ROE). An ROE $\delta\alpha = (\delta a, \delta\gamma, \delta e_x, \delta e_y, \delta i_x, \delta i_y)^T$ is composed of the



(a) Screenshot of 3D-visualization showing the TOM formation performing joint observation of the volcano Popocatépetl.



(b) Screenshot of the EOS, where one satellite of the TOM formation is observing the volcano Popocatépetl in Mexico.

Fig. 10: Visualization tools of the distributed testbed.

following elements: altitude difference δa , along-track separation $\delta\gamma$, relative eccentricity ($\delta e_x, \delta e_y$) and relative inclination ($\delta i_x, \delta i_y$). The relative eccentricity and inclination consist of two values, defining the amplitude and phase of each pendulum behaviour for the in-plane and out-of-plane motion [34, 35]. This resulted in the following formation for the three satellites oscillating with different phases:

$$a\delta\alpha_1 = \begin{pmatrix} 0 \\ 75km \\ 0 \\ 0 \\ 35km \\ 0 \end{pmatrix}, \quad a\delta\alpha_2 = \begin{pmatrix} 0 \\ 0 \\ 0 \\ 0 \\ 17.5km \\ -30.3km \end{pmatrix}, \quad a\delta\alpha_3 = \begin{pmatrix} 0 \\ -75km \\ 0 \\ 0 \\ 17.5km \\ 30.3km \end{pmatrix}.$$

This results for the first satellite $a\delta\alpha_1$ in an inclination difference of 0.29° , and for the second ($a\delta\alpha_2$) and third ($a\delta\alpha_3$) an inclination difference of 0.14° and for the Right Ascension of the Ascending Node (RAAN) difference of 0.25° .

In every update step the actual state, propagated by the simulation framework, was recorded and post-processed to calculate the absolute pointing accuracy during the target observation. For the

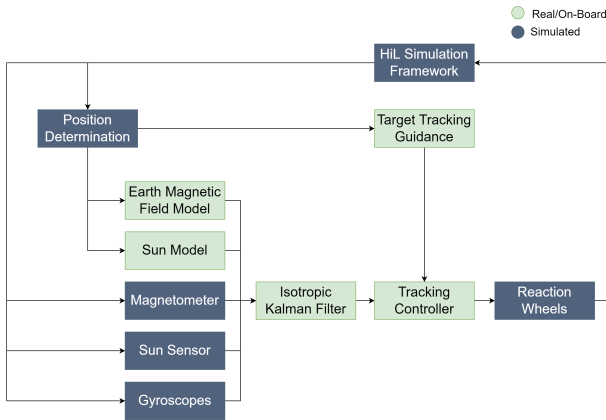


Fig. 11: Flowchart of the absolute tracking control loop test. In blue: simulated components, in green: real components running on-board.

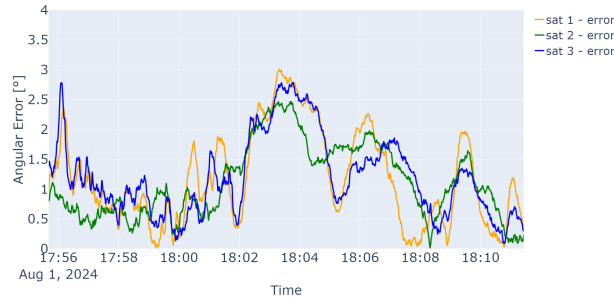


Fig. 12: Absolute pointing error of the TOM satellites in LLA pointing mode during the observation of the volcano Popocatépetl.

evaluation Systems Tool Kit (STK) served as reference, providing the required orientation of the satellites.

The result is shown in Figure 12, where the pointing error of all three satellites is plotted during the target observation. The satellites reach their maximum elevation with $e_{sat1_{max}} = 74.40^\circ$, $e_{sat2_{max}} = 69.56^\circ$, $e_{sat3_{max}} = 74.85^\circ$ at around 18:00. The absolute pointing error of all satellites stays below 3° during the whole observation time. Table 2 shows a statistical analysis with the standard deviation σ_p of the resulting pointing error for the different satellites. The graph shows that the pointing error decreases significantly around the time of maximum elevation (approx. 18:00). In the 3D visualization, it was observed that the pointing axis of the satellites crosses the observation target at this time, which leads to this reduction in the error.

The pointing error increases significantly after

Satellite	1	2	3
σ_p	0.75°	0.64°	0.67°

Table 2: Absolute pointing error analysis of all three satellites during overpass.

the maximum elevation and later reaches almost 3° . When analyzing the angle between the sun vector and the magnetic field vector in the Earth Centered Inertial (ECI) frame, we found that the two vectors converge. This convergence probably reduces the accuracy of the attitude determination, as the smaller angular separation between the sun and magnetic field vectors leads to information redundancy. Both sensors provide nearly similar data, which reduces the ability of the Kalman filter to accurately determine the satellite's attitude, especially in axes perpendicular to these vectors. The reduced observability and sensitivity for certain rotational axes leads to less accurate attitude estimations [36].

In general, the performance of the Kalman filter depends heavily on how well the sensor noise is modeled. In simulations, the noise characteristics may be too idealized or mismatched compared to real sensor behavior. Simulations are often based on simplified or conservative models of sensor noise, actuator limitations and external disturbances. This can lead to either overly optimistic or pessimistic performance estimates. For example, simulations may underestimate real-world disturbances or overestimate sensor noise while not fully capturing the complexity of non-linearities and sensor interactions, which may result in the filter performing better or worse in orbit than predicted. Given the limitations of purely simulated inputs, we recognize the need to further investigate the filter's performance with real sensor inputs. To achieve this, we plan to expand our air bearing-based testbed, as described in section 7.3 to incorporate real sensors and actuators into the test loop, allowing for a more realistic evaluation of system behavior. This will bring us closer to the actual conditions in orbit and provide more reliable insights into the filter's performance and resulting absolute pointing accuracy.

7.3 Extensions of Test Environment

As already mentioned in section 7.2, it is planned to adapt our distributed testbed with the air bearing-based testbed from Astrofein to include the real sensors and actuators in order to get a more realistic

estimation of the in-orbit performance of the Kalman filter and thus to better estimate whether the initial pointing accuracy of the three satellites is sufficient to apply the coordinated relative image-based control approach. The air-bearing testbed includes a Sun simulator, a Helmholtz cage and a camera tracking system from OptiTrack, requiring the implementation of interfaces to the simulation framework. Additionally, orbit scenarios have to be constructed as the roll- and pitch-axis are limited to ±20°.

Besides this, it is also planned to integrate the EOS within the air bearing-based testbed, where the OptiTrack measures the current attitude of the satellite and forwards it to the EOS to display the current area on Earth seen by the TOM payload camera. With this extension, multi-satellite tests can be performed in combination with the turntables, enabling the possibility to verify the coordinated observation in a formation, especially the transition from absolute to relative control. Additionally, this extension also allows to test the relative image-based attitude control approach in a closed-loop manner, including the simulation of the ISL. This will also help to test the automatism implemented on the AOCS for the joint observation mode and check if a proper timing in the mode transitions is considered.

Further extensions could include the integration of the real payload camera in the testbed. This can be realised in different ways, where a wireless connection to the camera will probably be the most flexible solution as it can then be integrated in each testbed configuration. In the planned concept, the payload camera would be placed in front of a screen, where the EOS displays the current view of the satellite, and the image data would be transmitted wirelessly to the payload computer. It is still to be investigated if sufficient transmission rates can be achieved with the wireless connection, and the additional transmission delays have to be quantified.

8. Photogrammetry Pipeline

The synchronous multi-view imaging provided by the TOM satellite formation allows for 3D reconstructions with unmatched time resolution via photogrammetric processing. As such, it is suitable for highly dynamical situations with quickly moving or transforming structures. A particularly relevant case of such a scenario that TOM focuses on is the reconstruction of ash clouds from volcanic eruptions.

Analogous to the visual servoing task presented in chapter 6, photogrammetric 3D reconstruction

is based on the same principles of feature detection, identification of correspondences and pose estimation. Unlike the former task, however, the image data does not need to be processed in real time and all calculations can be done after downloading the data via the ground station network. Thus, for this task, we are not restricted by rather limited processing resources on the satellite and can make use of well established photogrammetry pipelines that allow an automatic reconstruction from a series of pictures. After the aforementioned processing steps these pipelines continue with the triangulation of key points in 3D, that get densified to a more detailed point cloud and eventually result in the reconstruction as a mesh.

8.1 Pipeline selection

Both Agisoft Metashape and OpenMVG were originally considered as potential reconstruction pipelines for TOM. During testing, however, Metashape showed substantial problems in the case of only a small number of pictures from limited perspectives, resulting in highly distorted reconstruction results. In contrast to this, OpenMVG was able to produce reconstructions from only three images taken from similar perspectives. As this reflects the situation for our satellite formation, we expect TOM to be able to produce 3D captures from only a single combined image acquisition of all three satellites as a snapshot in time.

8.2 Simulations

Apart from the different boundary conditions on available computational power, another important difference to visual servoing is given by the substantially different optical properties of clouds and ground points. While the ground can generally be well represented by a closed surface, clouds are inherently gaseous and translucent which results in volume scattering.

The photogrammetric reconstruction of an ash cloud via an automated pipeline could already be demonstrated for a particular volcano eruption in [9]. To evaluate the specific camera, lens and formation setup planned for TOM, realistic artificial data sets were generated. The simulation environment created for this also allowed to examine additional potential limiting factors that might influence the result in practice.

8.2.1 Model

A realistic 3D model constructed in Blender builds the basis to generate the data sets for the simulations.

This model combines existing satellite images for the ground texture with a volumetric 3D model of clouds with highly detailed volumetric density data.

For the lighting of the scene, a HDRI skydome texture was used to simulate indirect lighting from atmospheric scattering, combined with a directional sun light as the main light source. The satellite formation got modeled by a set of three virtual cameras with positional, focal length and sensor parameters according to the situation in TOM with the correct scale with respect to the ground images used. Rendering the scene from each of the virtual cameras produces images suitable to be processed by the pipeline. As the virtual model enables to control recording and environmental parameters, the general suitability of the approach and influencing factors could be checked.

8.2.2 Simulation results

The simulations are subject to ongoing research. Even though further work has to be done on quantifying simulation results, the existing qualitative observations give already a lot of interesting insights for the reconstruction of clouds.

The images acquired by the cameras on TOM cover a ground area with a width of approximately 50 km. Clouds might therefore only cover a small fraction of the image area. Without specifying a region of interest in the picture most features found come from the texture of the ground. Since the texture of the ground often shows a much more detailed structure, it was found that the reconstruction of the cloud often benefits from the higher density of the features from the ground depicted around. On the other hand, trying to reconstruct a cloud without ground texture caused the reconstruction to fail in most examined instances. If this effect can be reduced by additional preprocessing needs to be further researched, but we expect the reconstruction of clouds to be much harder in regions with low details on the ground, e.g. on the ocean.

Studying existing satellite images during the selection of suitable ground textures for our simulation, it was found that clouds often get overexposed. This is due to the fact that there is often a big difference in the albedo of the ground to that of the cloud. As a consequence the pixel interior of the cloud silhouette gets saturated and shows no structure that could be used for feature detection. The simulations with two different values for the cloud albedo are shown in Figure 13. Even

though a reconstruction of the outer parts of a cloud were still possible in the simulation with saturated cloud interior, there are unreconstructable parts in the interior which typically include the cloud tops. As the cloud top height is of particular interest for predictions on the cloud behavior this is a critical issue that needs to be taken into account for in exposure control.

When reconstructing solid objects by photogrammetry, pictures from different positions showing the same spot on the object from quite different angles can be combined, as the features on the surface can often still be identified from the different perspectives. For clouds, much stronger sensitivity with respect to changes in perspective was observed. Images acquired from views with relative angles differing by more than 15° usually resulted in insufficient feature correspondences. This is not surprising, since the clouds do not possess a textured surface, but on clouds features can only result from lighting on the 3D density structure itself.

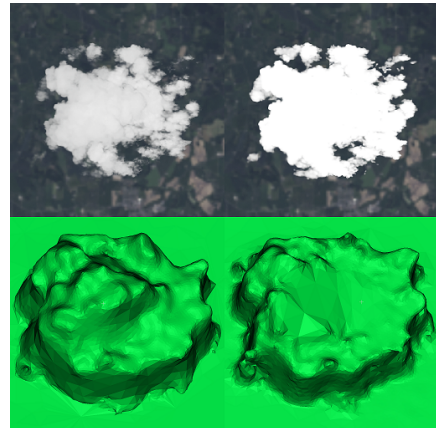


Fig. 13: Cloud renderings with different relative cloud albedo and the respective reconstructed meshes.

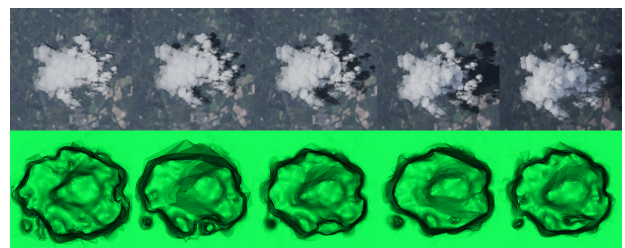


Fig. 14: Cloud renderings with different sun incident angle at 0, 10, 20, 40 and 60 degrees (left to right) and the respective reconstructed meshes.

For the same reason different lighting conditions resulting from different relative incident angles of sun light to the camera orientations, were also considered as factors potentially affecting the reconstruction. Using the simulation environment, this was tested by changing the sun incident angle while keeping the cameras at near nadir orientation. The results can be seen in Figure 14. Even though it is intuitively easier to identify cloud details in the images when the clouds are illuminated from the side, the effect on the reconstruction results were surprisingly minor with different angles resulting in different parts reconstructed in more detail and no clear optimum setting.

9. Image-based Attitude and Position Determination

To extend the applicability of image-based attitude control algorithms to further Earth observation missions, based on the existing relative visual servoing approach, an absolute one is developed: *absolute visual servoing* [37]. The goal of this approach is to enable the precise determination of the absolute attitude and position of the satellite based on images taken by the onboard camera.

Figure 15 shows an overview of the processing steps. Features are detected in the incoming image frames taken by the onboard camera. Then, they are compared and matched with ground control points (GCPs) stored in an onboard database.

In general, GCPs are structures on the Earth's surface with unique appearance in satellite imagery and with known geographic position. In the context of absolute visual servoing, these GCPs are features extracted by feature detection algorithms applied to satellite images in advance. To be able to determine their exact geographic position, the GCPs are detected in satellite images with given metadata that provide useful information about the geographic position of the displayed area. Based on this information, the exact geographic position of the GCPs can be determined. Afterwards, each GCP gets a unique signature generated by a feature description algorithm. Subsequently, the set of GCPs is filtered, so that only the GCP features remain that are most likely to be matched onboard. The remaining descriptor vectors are stored in an onboard database mapped with their absolute geographic position on Earth.

After the feature matching and validation process onboard the satellite, the absolute attitude and position of the satellite can be determined based on

the image positions and geographic positions of the matched GCP features in the current image frame. In photogrammetry, the procedure of determining the attitude and position of a camera based on point correspondences is often referred to as pose estimation. Thus, this term is also used in the following. Based on [38], a theoretical accuracy of less than 1 km for the absolute position error and of less than 0.1° for the angle error is to be expected [39]. The process of feature detection, description and matching as well as pose estimation in absolute visual servoing is illustrated in Figure 15.

To demonstrate the feasibility of the presented absolute visual servoing approach, the entire processing pipeline is tested. The GCP test database is created based on Landsat 8 image data [40] and covers approximately the region of Germany (approx. 550 km × 700 km). It contains 27740 GCPs, leading to 1.1 MB of required memory space. With the help of the Earth Observation Simulator (EOS), artificial satellite camera images from overpasses over Würzburg (Germany) are created. This artificial image data is used to test the attitude and position determination algorithm in a Processor-in-the-Loop (PiL) setup. The accuracy of the results is promising, but especially mismatched features sometimes lead to big determination errors. Therefore, one of the main goals of the ongoing research is to improve the matching step to increase reliability and accuracy of the algorithm.

In addition, the runtime of the different processing steps is measured. The results of the runtime measurements are shown in Table 3. While some processing steps are performed quite fast, further research needs to be conducted to improve the runtime of the detection&description and validation steps to enable the real-time application of absolute visual servoing.

Runtime	
Detection + Description [s]	0.621 ± 0.010
Matching [s]	0.158 ± 0.003
Validation [s]	1.52 ± 2.59
Pose Estimation [s]	7.51e-4 ± 0.54e-4
Total [s]	2.30 ± 2.60

Table 3: Mean value and standard deviation of the runtime for the different onboard processing steps of absolute visual servoing.

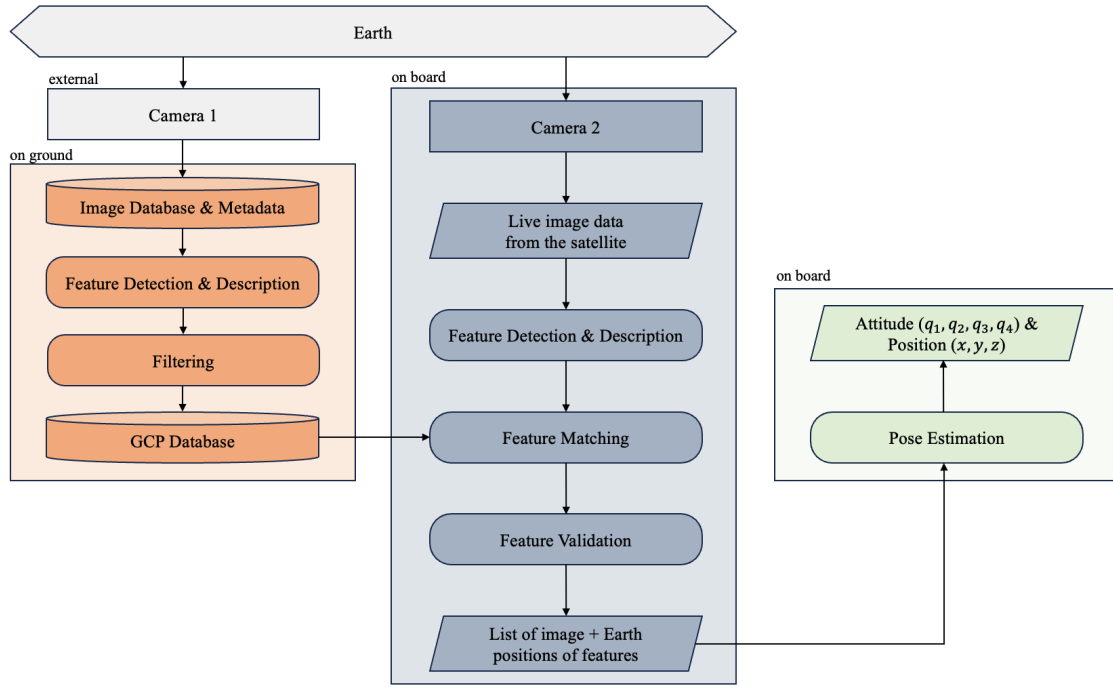


Fig. 15: Block diagram of the processes of feature detection, description and matching as well as pose estimation in absolute visual servoing [39].

10. Conclusion and Outlook

TOM will monitor ash clouds during volcanic eruptions with a satellite formation consisting of three CubeSats to provide image data for photogrammetric processing. The payload consisting of camera and payload computer addresses the challenges regarding exact image capture timing and synchronization. An image-based attitude control approach enables precise pointing for the joint tracking of observation targets.

Extensive simulations and HiL-tests already show promising results. Efforts continue to expand the existing test environment to evaluate further aspects of attitude control and formation flying in upcoming tests.

The three TOM satellites are now waiting in the cleanroom for their launch opportunity in 2025. Once operational, they will provide valuable image data for scientists to improve our understanding of our home planet Earth.

Acknowledgments

The authors thank all the collaborators for their contributions within the Telematics Earth Observation Mission (TOM), supported by the Bavarian Ministry of Economics and the Regional

Leaders Summit (RLS) for the cooperation in the Telematics International Mission (TIM). In addition, we gratefully acknowledge the support of the Elite Network Bavaria (ENB) for providing funds for the academic degree program “Satellite Technology”.

References

- [1] K. Schilling, “Perspectives for miniaturized, distributed, networked cooperating systems for space exploration,” *Robotics and Autonomous Systems*, vol. 90, pp. 118–124, 2017.
- [2] R. M. Millan, R. von Steiger, M. Ariel, S. Bartalev, M. Borgeaud, S. Campagnola, J. C. Castillo-Rogez, R. Fléron, V. Gass, A. Gregorio, D. M. Klumper, B. Lal, M. Macdonald, J. U. Park, V. Sambasiva Rao, K. Schilling, G. Stephens, A. M. Title, and J. Wu, “Small satellites for space science: a COSPAR scientific roadmap,” *Advances in Space Research*, vol. 64, no. 8, pp. 1466–1517, 2019. [Online]. Available: <https://www.sciencedirect.com/science/article/pii/S0273117719305411>
- [3] T. Zurbuchen, R. von Steiger, S. Bartalev, X. Dong, M. Falanga, R. Fléron, A. Gregorio, T. S. Horbury, D. Klumper, M. Küppers,

- M. Macdonald, R. Millan, A. Petrukovich, K. Schilling, J. Wu, and J. Yan, “Performing high-quality science on cubesats,” *Space Research Today*, vol. 196, pp. 11–30, 2016.
- [4] R. Sandau, *Novel ideas for nanosatellite constellation missions*. International Academy of Astronautics, 2012.
- [5] M. D’Errico, *Distributed space missions for Earth system monitoring*. Springer Science & Business Media, 2012, vol. 31.
- [6] K. Schilling, T. Tzschichholz, I. Motroniuk, A. Aumann, I. Mammadov, O. Ruf, C. Schmidt, N. Appel, A. Kleinschrodt, S. Montenegro *et al.*, “Tom: a formation for photogrammetric Earth observation by three cubesats,” in *4th IAA Conference on University Satellite Missions, Roma*, 2017.
- [7] A. Kleinschrodt, I. Mammadov, E. Jäger, J. Dauner, J. Scharnagl, and K. Schilling, “TOM/TIM Realization — A satellite EARTH Observation (EO) formation flying mission of three nano satellites for retrieving multi view stereoscopic data,” in *Proceedings of the 73th International Astronautical Congress. Paris, France: IAF*, 2022.
- [8] J. Jensen, J. Dauner, A. Kleinschrodt, I. Mammadov, P. Kamble, L. Elsner, and K. Schilling, “Cooperative Observations by Photogrammetric Methods with the TOM Satellite Formation,” in *Small Satellites Systems and Services (4S) Symposium*, 2024.
- [9] K. Zakšek, M. R. James, M. Hort, T. Nogueira, and K. Schilling, “Using picosatellites for 4-D imaging of volcanic clouds: proof of concept using ISS photography of the 2009 Sarychev peak eruption,” *Remote Sensing of Environment*, vol. 210, pp. 519–530, 2018.
- [10] S. Busch and K. Schilling, “Standardization approaches for efficient electrical interfaces of cubesats,” *integration*, vol. 3, no. 4, p. 5, 2016.
- [11] J. Scharnagl, R. Haber, V. Dombrovski, and K. Schilling, “Netsat — challenges and lessons learned of a formation of 4 nano-satellites,” *Acta Astronautica*, vol. 201, pp. 580–591, 2022.
- [12] T. Geiger, “Integration of vision-based attitude control and advanced camera driver software for the TOM satellite mission,” Master’s thesis, University of Würzburg, 2024.
- [13] L. Elsner, T. Petermann, M. von Arnim, and K. Schilling, “Pre-flight verification of the cubesat attitude control system for the QUBE mission,” 05 2024.
- [14] D. Vallado, P. Crawford, R. Hujasak, and T. Kelso, “Revisiting spacetrack report #3: Rev,” 08 2006.
- [15] L. Palacios and P. Gurfil, “Symplectic orbit propagation based on Deprit’s radial intermediary,” *Astrodynamic*, vol. 2, pp. 375–386, 12 2018.
- [16] ———, “Variational and symplectic integrators for satellite relative orbit propagation including drag,” *Celestial Mechanics and Dynamical Astronomy*, vol. 130, 04 2018.
- [17] C. G. Mayhew, R. G. Sanfelice, and A. R. Teel, “Quaternion-based hybrid control for robust global attitude tracking,” *IEEE Transactions on Automatic Control*, vol. 56, no. 11, pp. 2555–2566, 2011.
- [18] S. Hutchinson, G. D. Hager, and P. I. Corke, “A tutorial on visual servo control,” *IEEE transactions on robotics and automation*, vol. 12, no. 5, pp. 651–670, 1996.
- [19] F. Chaumette and S. Hutchinson, “Visual servo control. I. basic approaches,” *IEEE Robotics & Automation Magazine*, vol. 13, no. 4, pp. 82–90, 2006.
- [20] C. Cai, “6D visual servoing for industrial manipulators applied to human-robot interaction scenarios,” 2017.
- [21] J. Dauner, L. Elsner, O. Ruf, D. Borrman, J. Scharnagl, and K. Schilling, “Visual servoing for coordinated precise attitude control in the TOM small satellite formation,” *Acta Astronautica*, vol. 202, pp. 760–771, 2023. [Online]. Available: <https://www.sciencedirect.com/science/article/pii/S0094576522005409>
- [22] T. Tuytelaars, K. Mikolajczyk *et al.*, “Local invariant feature detectors: a survey,” *Foundations and trends® in computer graphics and vision*, vol. 3, no. 3, pp. 177–280, 2008.
- [23] F. Alhwarin, “Fast and robust image feature matching methods for computer vision applications,” Ph.D. dissertation, Bremen, Universität Bremen, Diss., 2011, 2011.

- [24] M. A. Fischler and R. C. Bolles, "Random sample consensus: a paradigm for model fitting with applications to image analysis and automated cartography," *Communications of the ACM*, vol. 24, no. 6, pp. 381–395, 1981.
- [25] H. Bay, T. Tuytelaars, and L. Van Gool, "SURF: speeded up robust features," *Lecture notes in computer science*, vol. 3951, pp. 404–417, 2006.
- [26] E. Rublee, V. Rabaud, K. Konolige, and G. Bradski, "ORB: an efficient alternative to sift or surf," in *2011 International conference on computer vision*. Ieee, 2011, pp. 2564–2571.
- [27] S. Leutenegger, M. Chli, and R. Y. Siegwart, "BRISK: binary robust invariant scalable keypoints," in *2011 International conference on computer vision*. Ieee, 2011, pp. 2548–2555.
- [28] A. Alahi, R. Ortiz, and P. Vandergheynst, "FREAK: fast retina keypoint," in *2012 IEEE conference on computer vision and pattern recognition*. Ieee, 2012, pp. 510–517.
- [29] OpenCV-Team. (2020) About-OpenCV. [Online]. Available: <https://opencv.org/about/>
- [30] T. Petermann, E. Jäger, L. Elsner, D. Pearson, G. Dietl, and K. Schilling, "A distributed hardware-in-the-loop testbed for attitude control of small communication satellites," in *Proceedings of IEEE Space Hardware and Radio Conference (SHaRC)*, *in press*, 2025, pp. 1–4.
- [31] CS-Group, "Orekit: an accurate and efficient core layer for space flight dynamics applications," www.orekit.org (accessed 2024-04-10).
- [32] "Hipparchus: a mathematics library," www.hipparchus.org (accessed 2024-04-10).
- [33] D. Friesen, "Development of an Earth observation simulator," Master's thesis, University of Würzburg, 2023.
- [34] A. W. Koenig, T. Guffanti, and S. D'Amico, "New State Transition Matrices for Relative Motion of Spacecraft Formations in Perturbed Orbits," in *AIAA/AAS Astrodynamics Specialist Conference*. Long Beach, California: American Institute of Aeronautics and Astronautics, Sep. 2016. [Online]. Available: <https://arc.aiaa.org/doi/10.2514/6.2016-5635>
- [35] S. D'Amico and O. Montenbruck, "Proximity Operations of Formation-Flying Spacecraft Using an Eccentricity/Inclination Vector Separation," *Journal of Guidance, Control, and Dynamics*, vol. 29, no. 3, pp. 554–563, May 2006. [Online]. Available: <https://arc.aiaa.org/doi/10.2514/1.15114>
- [36] S. Esteban, J. Giron-Sierra, O. Polo, and M. Angulo, "Signal conditioning for the kalman filter: application to satellite attitude estimation with magnetometer and sun sensors," *Sensors*, vol. 16, p. 1817, 10 2016.
- [37] J. Dauner, J. Redelbach, L. Elsner, I. Mammadov, and K. Schilling, "Absolute visual servoing for precise Earth target pointing onboard small satellites," in *Proceedings of the 74th International Astronautical Congress (IAC)*, Baku, Azerbaijan, 2023.
- [38] W. Förstner and B. P. Wrobel, *Photogrammetric computer vision*. Springer, 2016.
- [39] J. Redelbach, "Prototype implementation of image-based attitude and position determination for absolute visual servoing," Internship Report, University of Würzburg, 2024.
- [40] U. S. G. Survey, "Landsat 8," (online; accessed 12-September-2023). [Online]. Available: <https://www.usgs.gov/landsat-missions/landsat-8>